crystals

MDPI

Article

Three-Dimensional Gradient Metamaterial Devices Coupled with Phononic Crystals for Acoustic Enhancement Sensing

Xinsa Zhao, Guodong Hao, Yu Shang * and Jianning Han *

School of Information and Communication Engineering, North University of China, Taiyuan 030051, China; xinsazhao@163.com (X.Z.); adeneogdhao@163.com (G.H.)
* Correspondence: yushang@nuc.edu.cn (Y.S.); hanjn46@nuc.edu.cn (J.H.)

Abstract: Conventional acoustic systems exhibit a difficulty in sensing weak acoustic fault signals in complex mechanical vibration environments. Therefore, it is necessary to develop an acoustic sensing mode and a corresponding functional device with pressure amplification. This paper proposes a three-dimensional device, coupling gradient acoustic metamaterials (GAM) with phononic crystals (GAM–PC). The strong wave compression effect coupled with the phononic crystal equivalent medium mechanism is utilized to achieve the enhancement of weak acoustic signal perception at the target frequency. The superior amplification capability of the GAM–PC structure for the amplitude of loud signals is verified by numerical simulations and experiments. Moreover, the GAM–PC structure has a narrower bandwidth per slit, making it more frequency selective. Furthermore, the structure can separate different frequency components. This work is expected to be applied to signal monitoring in environments with strong noise.

Keywords: gradient structure; phononic crystals; acoustic metamaterials; acoustic enhancement sensing

Citation: Zhao, X.; Hao, G.; Shang, Y.; Han, J. Three-Dimensional Gradient Metamaterial Devices Coupled with Phononic Crystals for Acoustic Enhancement Sensing. *Crystals* **2023**, *13*, 1191. https://doi.org/10.3390/cryst13081191

Academic Editor: Luis M. Garcia-Raffi

Received: 29 June 2023
Revised: 26 July 2023
Accepted: 29 July 2023
Published: 31 July 2023

1. Introduction

Pressure amplification acoustic systems are widely used for sensing weak acoustic fault signals in complex mechanical vibration environments, such as mechanical structure health monitoring [1,2], sound source localization [3], and acoustic holographic imaging [4]. Conventional sound source detection is typically achieved by using microphone arrays, but the effectiveness of this approach is fundamentally limited by the physical characteristics of the microphone sensor diaphragm [5,6]. Moreover, both microphone array-based techniques and single-microphone systems may fail to detect sound signals that are drowned out by strong background signals. Amidst strong background noise, pre-amplification of weak sound sources and filtering processing are effective methods to enhance the signal-to-noise ratio for sensing under complex conditions. Therefore, there is an urgent need to develop sensing modes and functional devices with pressure amplification to overcome the limitations of current acoustic sensing technologies.

Over the last two decades, acoustic metamaterials have enabled the development of functional devices, including acoustic cloaks of invisibility [7,8], super-resolution imaging [9,10], acoustic metasurfaces [11–13], metamaterial resonators [14,15], insulators and absorbers [16–19], nonreciprocal acoustics [20,21], and topological metamaterials [22,23], owing to their unique ability to modulate acoustic wave propagation. Acoustic metamaterials have been expected to advance acoustic sensing and detection technology through applicable devices which are compatible with existing electroacoustic conversion sensors [24–26]. Therefore, the development of metamaterial devices is particularly critical.

In recent years, there has been a surge of interest in a new type of acoustic metamaterial structure known as gradient refractive index (GRIN) due to its potential for enhancing acoustic sensing capabilities and controlling the capture of acoustic rainbows [27]. In contrast to periodic metamaterials, metamaterials or media with GRIN show flexible control of acoustic waves [28]. The findings indicate that gradient acoustic metamaterials

(GAM) can achieve acoustic rainbow trapping (ART) [29], which refers to trapping broadband acoustic energy at multiple locations and selectively focusing it according to its frequency, implying that GAM can be customized for capturing weak signals. Furthermore, several metamaterial-based devices have been developed to enable acoustic wave compression and acoustic field amplification, which can improve the detection of weak acoustic signals [30–32] and facilitate the development of acoustic sensors which are suitable for many applications. In 2014, Chen performed a systematic theoretical analysis of gradient acoustic metamaterial structures (GAM), which achieve significant ART effects and enhance acoustic sensing through acoustic compression and pressure amplification [28]. In 2019, Huang et al. proposed an improved gradient structure (AMM) with gradient profile, thickness, and gap width, achieving a remarkable acoustic gain of more than an order of magnitude [33]. In 2022, Chen proposed a gradient metamaterial coupled with space-coiling structure (GAM–SCS) to achieve pressure amplification and acoustic localization [34]. Despite the growing research in enhanced signal sensing, current GAM approaches for obtaining acoustic enhancement are mainly based on 2D cells, which may not facilitate practical engineering applications. Ideally, these cells necessitate infinite or exceedingly large dimensions in the third direction.

The properties of subwavelength phonon crystal (PC) arrays provide ideas for solving this problem. PC arrays can be constructed with the characteristics of high refractive index media [35–37]. Therefore, in this work, a device made from axisymmetric three-dimensional gradient metamaterials which incorporate phononic crystals (GAM–PC) is proposed, which has a gradient profile, a gradient plate thickness, and a gradient gap width along the axis of the wave propagation direction. The enhanced acoustic amplification capability of the proposed GAM–PC device was verified by numerical simulations and experiments without losing the bandwidth of the captured acoustic signal per gap. In addition, it had superior multi-band acoustic filtering capability, making it well suited for signal monitoring in noisy and complex environments.

The structure of this paper is as follows. In Section 2, the GAM–PC structure is designed and the properties of the model are deduced by numerical calculations. In Section 3, finite element simulations of the model are performed to verify the acoustically enhanced properties of the designed GAM–PC structure, and the operating frequency bandwidth characteristics of the GAM–PC structure are also investigated. In Section 4, the performance of the GAM–PC structure is experimentally tested to verify its ability to acoustically enhance and separate different frequency components. In Section 5, the research results of the entire study are summarized.

2. Materials and Methods

2.1. Model Structural Design

GAMs are composed of spatially varying unit cells or media. Their effectiveness in amplifying sound signals is attributed to the combination of gradient refractive indices and the strong wave compression effect [28]. Incident acoustic waves of different wavelengths are captured at different locations for enhancement. Nevertheless, in certain cases, the limited maximum effective index may hinder the perception of weak acoustic fault signals. To enhance the detection capability limit of the maximum detectable pressure in acoustic sensing systems, a three-dimensional GAM–PC structured device, as shown in Figure 1a, was designed by gradually converting the abrupt signal into a propagating wave, inspired by Li et al. [24]. Figure 1b presents a side view of the GAM–PC. The structure, as depicted in the lateral cross-sectional view of Figure 1c, was comprised of an array of 22 cylindrical plates. Taking the position of the lower left corner of the first plate as the coordinate origin, the first cylindrical plate was constructed with r = 4 mm. The plate thickness was c = 2 mm, and the gap between the plates was set to a = 8 mm. The radii of the 2nd to 22nd cylindrical plates were uniformly incremented in steps of t = 4 mm until the radius of the 22nd cylindrical plate was R = 88 mm. The 22 plates formed were rotated 360 degrees to form a three-dimensional GAM structure. A phononic crystal structure

was embedded for coupling between the gaps of the 22 cylindrical plates of the GAM. Within the air gaps of the structure, a rectangular solid of length b = 6 mm and width e = 2 mm was immersed centrally within the rectangular air region of length a = 8 mm and width r = 4 mm, to construct a phononic crystal unit with the center as the axis of symmetry. The number of phononic crystal units was incremented by one between each pair of neighboring gaps. For the same gap, the distance between the phononic crystal units was d = 2 mm. Three-dimensional conical-structured GAM–PC were obtained by rotation.

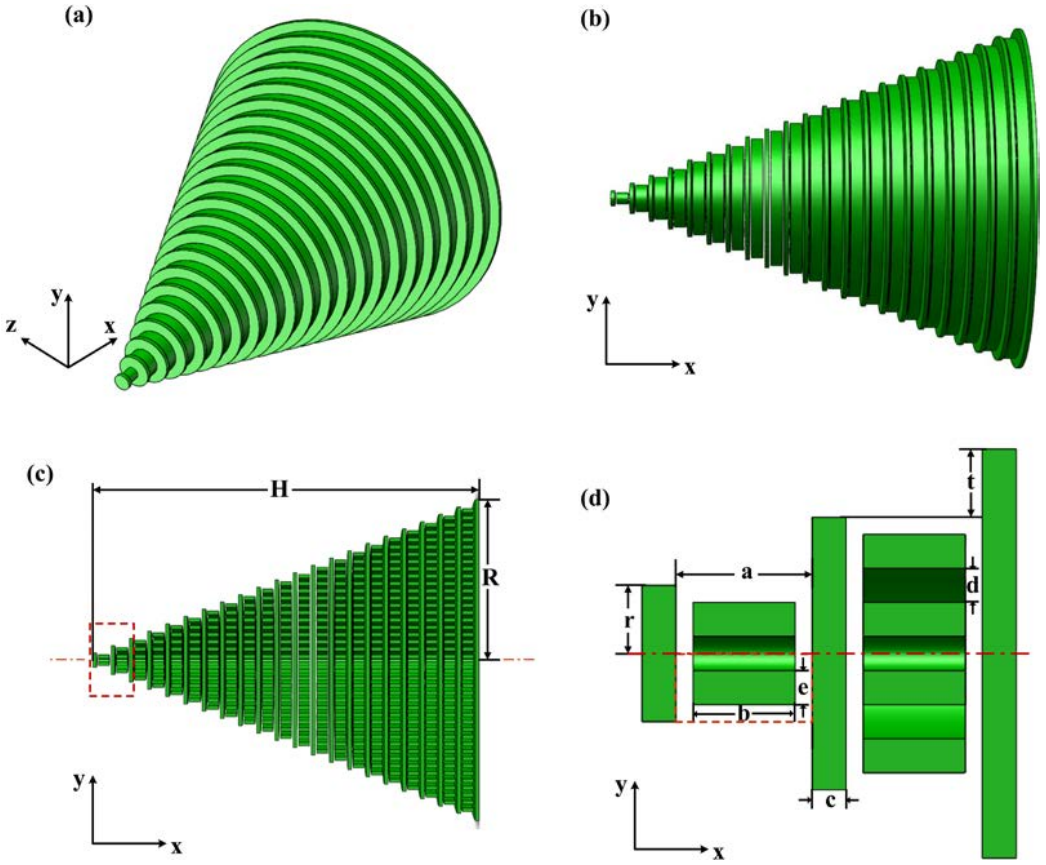

Figure 1. (**a**) Three-dimensional view of GAM–PC; (**b**) Side view of GAM–PC; (**c**) The lateral cross-sectional view of GAM–PC; (**d**) Enlarged view of GAM–PC unit.

2.2. Theoretical Analysis

Based on the characteristics of GAM–PC, a numerical model was developed to analyze their performance theoretically. Chen [28] et al. used the equivalent medium theory to derive the mechanism for enhancing acoustic pressure in gradient structures. The effective mass density ρ and bulk modulus K can be expressed as

$$\rho = \frac{\rho_{res}\rho_{eff}}{(1-F_r)\rho_{res} + F_r\rho_{eff}} \tag{1}$$

$$K = \frac{K_{res}K_{eff}}{(1-F_r)K_{res} + F_rK_{eff}} \tag{2}$$

where F_r is the filling rate of the parallel plate. In Section 2, the constructed models of GAM–PC were fabricated using photosensitive resin, which had a density of $\rho_{res} = 1130$ kg/m^3 and a bulk modulus of $K_{res} = 2.65$ GPa. The air had a density of $\rho_{air} = 1.2$ kg/m^3 and a bulk modulus of $K_{air} = 1.42 \times 10^5$ Pa. As revealed by analyzing the cross-sectional angle along the central axis position, the conical structure formed by the PC arrangement offered a larger propagation path for sound compared to uniform air when the sound waves entered

between the two plates, effectively reducing the sound propagation speed [38]. Based on the geometry of the phononic crystal unit and parameter settings (Table 1), the calculated crystal band structure is shown in Figure 2, where the lowest band is located below the sound cone (blue part). The coefficient of reduction of the equivalent speed of sound between the two plates c_{eff} (filling the PC structure) with respect to c_{air} (the speed of sound in air) can be expressed in terms of the effective refractive index. The dispersion in the lowest frequency band is linear over a wide bandwidth from 0 to 13 kHz (indicated by the dashed line). The slope k of this linear fit is

$$k = c_{air}/n_{eff} \tag{3}$$

where n_{eff} is the effective refractive index of the PC. It is noteworthy that the effective refractive index of the PC medium constructed between the two plates in this band range is higher than that of uniform air (n_{eff} = 1.97 > 1). This is crucial for the GAM–PC to further enhance the refractive index of GAM. The function of GAM–PC width can be expressed as

$$z(x) = 2tx/(c + a) + r \tag{4}$$

where x denotes the direction as shown in Figure 1d, and a, c, and r are all geometric parameters in Figure 1d.

Table 1. Values of geometric parameters of the GAM–PC.

Parameters	H	R	r	a	c	t	b	d	e
Values (mm)	212	88	4	8	2	4	6	2	2

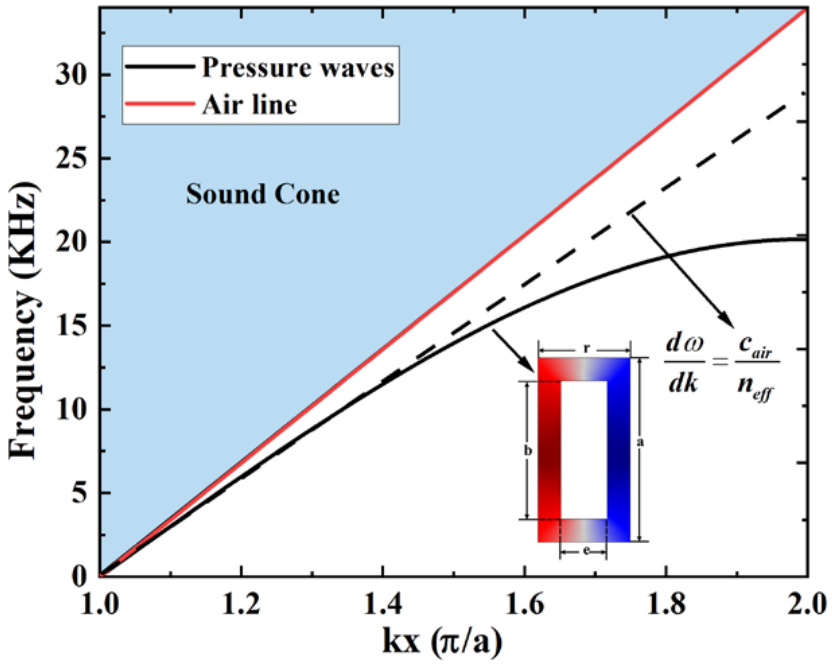

Figure 2. Dispersion diagram.

In acoustic metamaterials, the effective refractive index can be used to quantify the increase in the wavenumber of guided waves caused by the medium. For GAM–PC, the transverse wave vector can be expressed as

$$k_x = 2\pi f\sqrt{\frac{\rho}{K}} \tag{5}$$

For the GAM–PC structure, combining Equation (5) with Equation (3), the effective refractive index of the metamaterial can be determined as follows:

$$n_{GAM-PC}(x,f) = \sqrt{n_{eff} + \frac{K_{eff} \cdot \rho_{eff}}{\rho \cdot K}} \left(\tan\left[2\pi f \cdot \frac{z(x)}{2} \cdot \sqrt{\frac{\rho}{K}} \right] \right)^2 \tag{6}$$

where K_{eff} represents the equivalent bulk modulus of PC, and ρ_{eff} represents the equivalent density of PC. Simultaneously,

$$\frac{K_{eff} \cdot \rho_{eff}}{\rho \cdot K} \approx (1 - F_r)^2 \tag{7}$$

F_r exhibits a linear increase with the x-axis direction of the GAM–PC, aligning with the characteristics of GAM without the incorporation of PC structures. However,

$$\sqrt{\frac{\rho}{K}} \approx \sqrt{\frac{\rho_{eff}}{K_{eff}}} = c_{eff} < c_{air} \tag{8}$$

resulting in a reduced magnitude of refractive index variation per gap for the GAM–PC compared to GAM. As a result, n_{GAM-PC} exhibits a higher and more smoothly varying refractive index compared to that of conventional GAM. As the refractive index of the material is enhanced, the amplitude of the acoustic wave also increases. Based on the aforementioned equation, the relationship between the sound pressure amplitude and the input frequency along the x-axis is as follows:

$$P_{GAM-PC}(x,f) = \frac{\sqrt{2\pi \cdot \rho_{eff} f} \cdot \sqrt[4]{1 - n_{GAM-PC}^{-2}}}{\cos\left[\arctan\left(\rho \cdot \rho_{eff}^{-1} \sqrt{n_{GAM-PC}^2 - 1} \right) \right]} \tag{9}$$

Owing to the incorporation of the PC structure in the gap between the two plates in GAM–PC, as compared to conventional GAM, there is an increase in both n_{GAM-PC} and the PC equivalent density ρ_{eff}.

3. Simulation Analysis of GAM–PC

To characterize the acoustic response of the metamaterial, for this paper, we constructed and meshed the 3D structure within the acoustics module (pressure acoustics) of COMSOL Multiphysics v6.0. Figure 3 displays the partial meshing grid of the model. The blue area was set as the sound wave exit port. In the air medium, the structure was treated as a rigid body, and the boundary was set as a hard acoustic field boundary (RB). A plane wave with a set amplitude of 1 Pa was utilized as the incident acoustic wave, entering from the x-angle direction. A perfectly matched layer (PML) was placed on the outside of the incident plane wave to absorb the reflected acoustic wave, as shown in the yellow area of Figure 3. To minimize the influence on the model sound field during the experiment, a microelectromechanical system microphone (MEMS-MIC) was positioned at the edge of the gap to detect the acoustic signal. In this study, the point probes were set at the 14th, 16th, 18th, and 20th air gap positions to observe the acoustic enhancement phenomenon occurring between the air gaps. The pressure gain value (PG) serves as a crucial indicator of the acoustic enhancement effect and is defined as PG = PM/PF [23]. Here, PM denotes the sound pressure amplitude added to the metamaterial structure, while PF indicates the sound pressure amplitude in the free sound field. To compare and analyze the effect of the gradient structure with and without the PC structure on acoustic enhancement, a conventional GAM structure with the same geometric parameters and simulation environment but without phonon crystals was constructed. Frequency domain simulations were performed for GAM–PC and GAM.

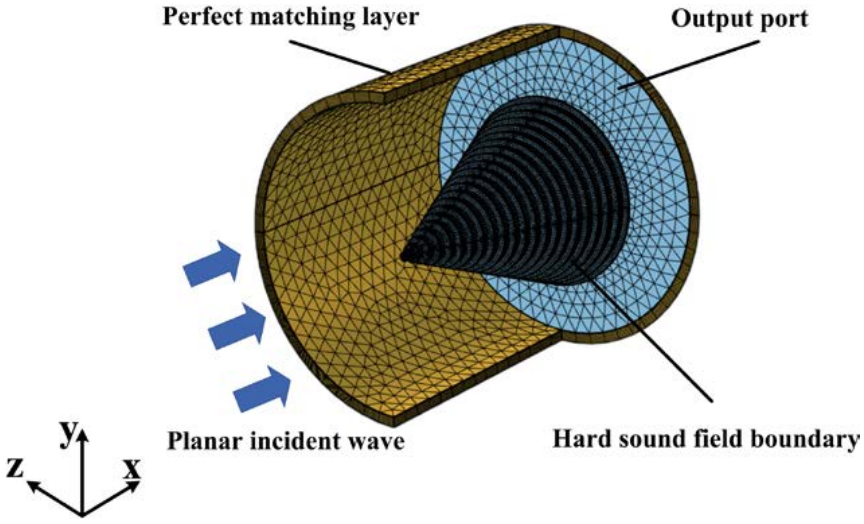

Figure 3. Schematic diagram of model section meshing.

Simulation results yielded the center frequencies of the 14th, 16th, 18th, and 20th air gaps of the GAM–PC structure at 1549 Hz, 1358 Hz, 1211 Hz, and 1095 Hz, respectively. Figure 4a–d illustrates the overall sound pressure distribution at these frequencies and the sound energy localization at specific plate gaps. For comparison, Figure 5a–d shows the sound pressure distribution at the center frequency of the GAM without phonon crystal structure at the same gap position. The results demonstrate that the proposed GAM–PC structure in this study effectively localizes the acoustic energy around the structure at a specific central position of the plate. Furthermore, it can achieve the capture and enhancement of the acoustic signal at a specific frequency. Figure 6 presents the absolute sound pressure gain between different air gaps of the GAM–PC and GAM structures. The sound pressure amplitudes amplified by the GAM–PC structure at the 14th, 16th, 18th, and 20th gaps were 85.9 times, 101.8 times, 116.9 times, and 119.5 times, respectively. At the corresponding positions, the amplified sound pressure amplitudes of the GAM structure were 45.1 times, 51.2 times, 56.8 times, and 62.9 times, respectively. The comparison demonstrates that GAM–PC performs better pressure amplification than GAM, and the concentrated acoustic energy with high energy density is more evident than in GAM. This finding is consistent with the theoretical derivation above, indicating that GAM–PC can effectively amplify acoustic signals. Compared to the acoustic metamaterial (AMM) proposed by Huang et al. in 2019 [33], which exhibited a structural amplification of 30 times, the acoustic pressure amplification achieved in the present study is significantly improved.

From the microscopic analysis, when the acoustic wave propagates through the metamaterial structure, different gaps in the capture of acoustic signals corresponding to various frequencies occur due to the gradient structure between the two partitions filled with PC structure. Simultaneously, the periodic structure of phononic crystals affects the propagation of phonons, resulting in a Bragg diffraction effect [39]. Similar to Bragg diffraction in photonic crystals, this effect limits the propagation of acoustic waves in specific directions, thereby increasing the refractive index of the acoustic waves. As sound waves are reflected and scattered within phononic crystals, an interference effect is generated by the sound waves traversing different paths. In certain cases, this interference effect enhances the amplitude of the acoustic wave, consequently increasing the energy density of the acoustic wave. The sound waves pass through the PC structure and reach the central gap portion of the structure. Resonance is formed in conjunction with the rigid boundary at the end of the gap, resulting in an enhanced amplitude.

Secondly, as depicted in Figure 6a, the maximum pressure ratio frequency of the GAM–PC (1549 Hz) was lower than that of the GAM (2114 Hz) at the same position (14th gap), enabling the GAM–PC to operate at a lower frequency. Thirdly, the resonance

bandwidth of GAM–PC (black line) was narrower than that of GAM due to the strong coupling effect. For narrow-band signal amplification, the narrow resonant bandwidth is preferable to the wide resonant bandwidth. The resonant bandwidth is tuned by the wave propagation distance in the phonon crystal structure. Increasing the wave propagation distance in the spatial structure results in a narrower resonant bandwidth, while a wider bandwidth is achieved with a shorter propagation distance.

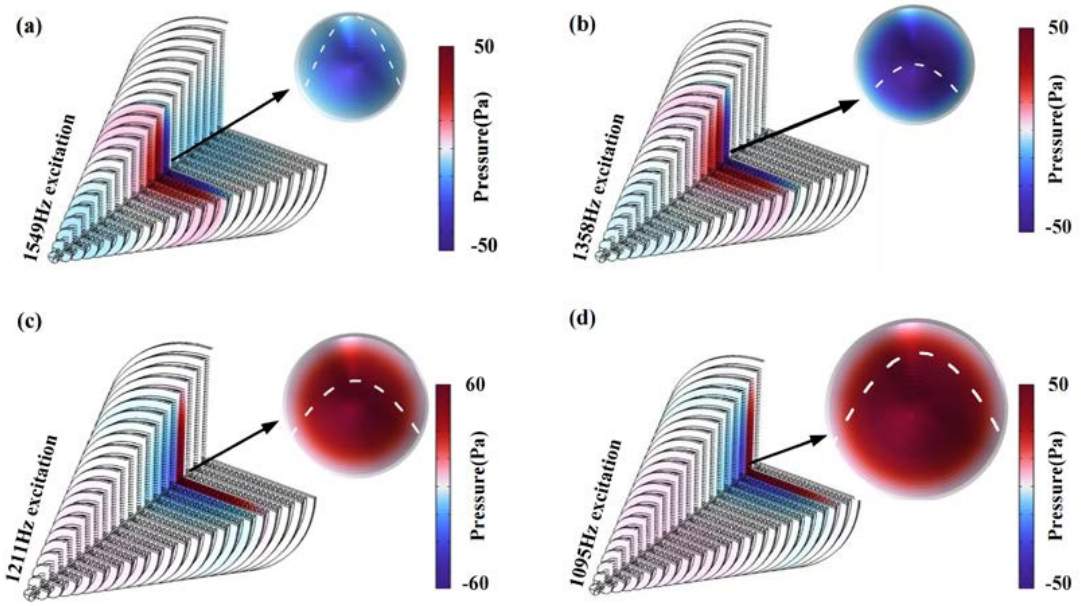

Figure 4. Overall sound pressure distribution in different air gaps and sound energy localizations in specific plate gaps of GAM–PC structures with PCs: (**a**) the 14th air gap at 1549 Hz; (**b**) the 16th air gap at 1358 Hz; (**c**) the 18th air gap at 1211 Hz; (**d**) the 20th air gap at 1095 Hz.

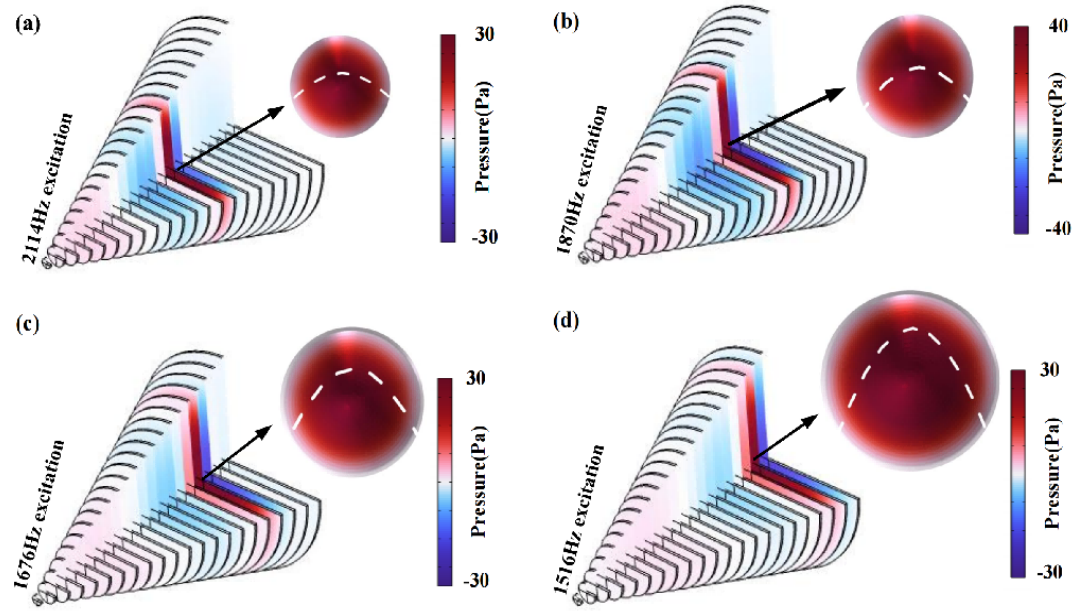

Figure 5. Overall sound pressure distribution in different air gaps and sound energy localizations in specific plate gaps of GAM structures without PCs: (**a**) the 14th air gap at 2114 Hz; (**b**) the 16th air gap at 1870 Hz; (**c**) the 18th air gap at 1676 Hz; (**d**) the 20th air gap at 1516 Hz.

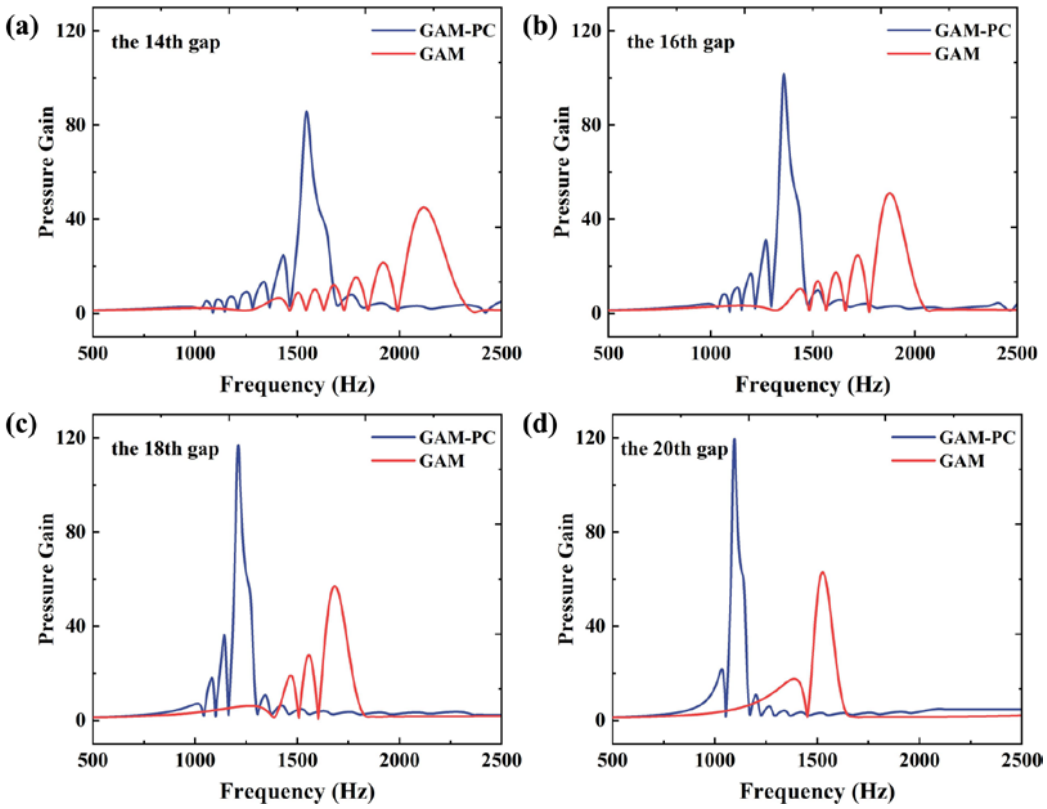

Figure 6. Absolute sound pressure gain between different air gaps of GAM–PC structure and GAM structure: (**a**) the 14th air gaps; (**b**) the 16th air gaps; (**c**) the 18th air gaps; (**d**) the 20th air gaps.

Additionally, the proposed GAM–PC device can operate over a wide bandwidth, which can be easily adjusted by changing the measurement position. Therefore, the resonant frequencies in each air gap of the GAM–PC were calculated. Firstly, the center frequencies of each air gap (from the 7th to the last air gap) of the GAM–PC structure (F_{Theory} in Hz) and the GAM structure (f_{Theory} in Hz) were calculated by Equation (9) and are listed in Table 2. Subsequently, the corresponding simulated values of F_{FEM} (Hz) and f_{FEM} (Hz) for the GAM–PC structure and the GAM structure were also obtained by simulation. The simulated operating frequencies of the GAM–PC ranged from 2948 Hz to 1048 Hz (approximately 1900 Hz bandwidth) across channels 7 to 21. The GAM operated from 3484 Hz to 1470 Hz (about 2000 Hz bandwidth) across channel 7 to channel 21. In comparison, the operating bandwidth of GAM–PC was narrower, but GAM–PC could operate at a lower frequency at the same scale. It was observed that the calculated theoretical values and the center frequency obtained by simulation were basically the same. However, these values cannot be applied in practical applications due to the necessity of considering thermal viscous losses and impedance in real environments.

Table 2. Center frequencies of each air gap obtained from calculations and simulations for GAM–PC structure and GAM structure.

Air Gaps	7th	8th	9th	10th	11th	12th	13th	14th	15th	16th	17th	18th	19th	20th	21th
F_{Theory} (Hz)	2946	2635	2378	2128	1943	1790	1662	1548	1443	1358	1282	1211	1151	1096	1048
f_{Theory} (Hz)	3481	3363	3127	2860	2634	2431	2258	2113	1984	1871	1782	1677	1598	1515	1470
F_{FEM} (Hz)	2948	2636	2378	2130	1944	1790	1662	1549	1444	1358	1282	1211	1150	1095	1048
f_{FEM} (Hz)	3484	3364	3128	2860	2634	2432	2260	2114	1984	1870	1780	1676	1598	1516	1470

4. Experimental Analysis of GAM–PC

An experiment was conducted in this study to evaluate the perceptual performance of the proposed GAM–PC in response to the actual special signals. Figure 7 illustrates the experimental setup and scenario. The experiments were conducted in an anechoic chamber, where acoustic waves from the loudspeaker were connected to the metamaterial device from free space. With the tip position of the GAM–PC structure as the reference, the loudspeaker was positioned at a distance of D = 0.7 m from the reference position. The output acoustic signal was a software-generated harmonic signal. Microphones were used to simultaneously collect the output signals from the reference microphones external to the GAM–PC and from multiple sensing microphones internal to the GAM–PC. The acoustic measurement device utilized in this study was a MEMS-MIC (model: S15OT421-005, sensitivity: −42 dB, amplification gain of 66), which was placed at the central edge of the gap to detect the acoustic signal.

Figure 7. Schematic diagram of the experimental setup.

4.1. Acoustic Enhancement

The microphone outputs obtained through the positions of gaps 14, 16, 18, and 20 are shown in Figure 8. The experimental results show that the actual gain was mostly between 20 and 35, defined as the ratio of the microphone output at each gap to the reference microphone output outside the GAM–PC. At certain gaps, the acoustic amplification was significantly lower than at other locations because the acoustic spot of the adjacent gap was split and covered both gaps. Deploying microphones in the gaps does not significantly interfere with the sound field; thus, the experimental gain could remain high, i.e., more than one order of magnitude. The amplification gain in high-frequency sound is more stable and larger. For gap 14, the GAM–PC center frequency measured in the simulation was 1549 Hz, and the amplification gain was 85.9. The GAM–PC center frequency measured in the experiment was 1490 Hz, and the amplification gain was 32.68. It can be observed that there was a small frequency shift in the peak frequency in the experiment, mainly caused by mechanical processing and measurement errors. There were discrepancies between the numerical and experimental results, which can be attributed to two main reasons. The first reason is that the resonant frequency in the gas cavity may not have matched the frequency of the maximum pressure ratio due to the strong wave compression effect. The second is that the coupling effect between the GAM and PC structures was weakened by viscous loss in practical applications. As a result, the maximum pressure ratio of the GAM–PC in the experiment was lower than that in the simulation. The viscous loss cannot be ignored when introducing a spatial PC structure. Theoretically, better pressure amplification can be achieved by increasing the length of the PC channel, but this also leads to an increase

in viscous loss. Consequently, there is a trade-off effect between pressure amplification and viscosity.

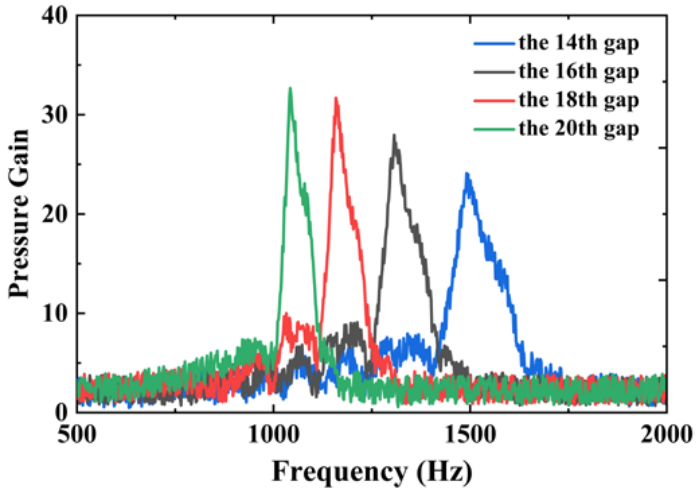

Figure 8. Measured values of pressure gain with different gaps.

4.2. Multi-Frequency Component Separation

To evaluate the capability of the proposed GAM–PC structure to separate multi-frequency composite signals, the propagation stop position and acoustic gain of swept-frequency acoustic waves were tested and analyzed to obtain the time domain response curves of different air gap centers selected in GAM–PC. A harmonic signal decomposition test was performed by inputting multi-frequency harmonic signals to the GAM–PC and observing the acoustic response in different gaps in the GAM–PC. This paper used loudspeakers to simulate the harmonic signals generated by vibrations as follows:

$$P(t) = \cos(2\pi \times f_0 \times t) + \cos(2\pi \times f_1 \times t) + \cos(2\pi \times f_2 \times t) + \cos(2\pi \times f_3 \times t) \quad (10)$$

where the target frequencies were f_0 = 1549 Hz, f_1 = 1358 Hz, f_2 = 1211 Hz, and f_3 = 1095 Hz. Figure 9a,b shows the time and frequency domain signals collected from a single microphone without the GAM–PC structure. The acoustic signals acquired through the free space of the structure without GAM–PC in Figure 9b demonstrate that three frequency components were prominent. The acoustic signals inside the 14th, 16th, 18th, and 20th air gaps received using MEMS-MIC are depicted in Figure 9c,e,g,i, respectively. Figure 9d,f,h,j shows the signals collected by the four microphones at different gaps (gaps 14, 16, 18, and 20) of the GAM–PC. As observed, only the signal of its own characteristic operating frequency was significantly enhanced for each channel, while the signals of other frequencies were not amplified. This finding suggests that GAM–PC possesses a more distinct frequency selectivity for each gap during the acoustic signal amplification. Sound waves of different frequencies were detected by microphones in various gaps, enabling spatial separation of distinct frequency sound signals. This real-time and uninterrupted multi-frequency component separation helps to extract and analyze target frequency signals in complex noise environments. Considering the quantitative calibration of the amplification of different frequency components, the structure is anticipated to be applicable in weak sound localization technology by normalizing the amplification of different gaps.

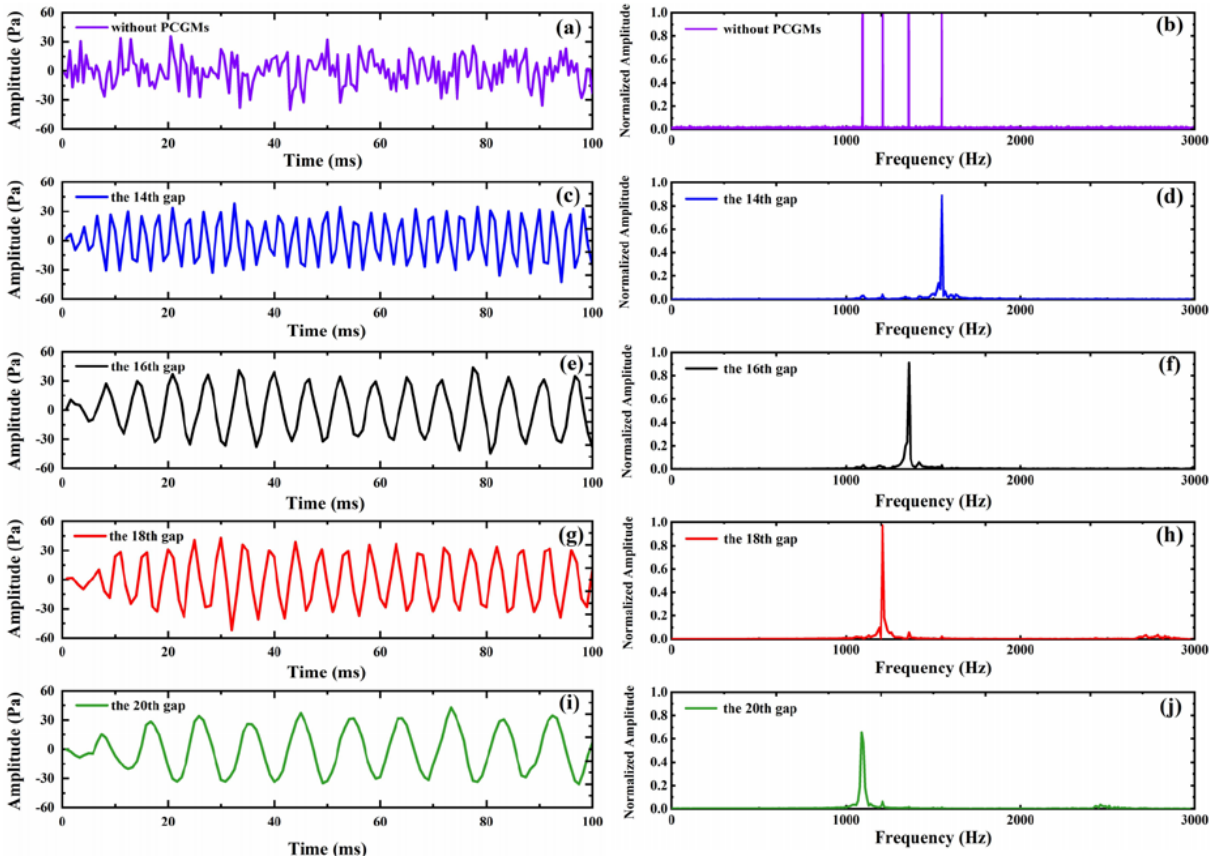

Figure 9. GAM–PC structure frequency separation function: (**a**) microphone output signal without GAM–PC structure; (**b**) output signal frequency response without GAM–PC structure; (**c**,**e**,**g**,**i**) microphone output signal of the 14th, 16th, 18th, and 20th gaps of the GAM–PC structure; (**d**,**f**,**h**,**j**) output signal frequency response of the 14th, 16th, 18th, and 20th gaps of the GAM–PC structure.

5. Conclusions

This work proposes a novel three-dimensional GAM–PC conical structure device, which utilizes the strong wave compression effect coupled with the phonon crystal equivalent medium mechanism to enhance the weak acoustic signal amplitude at the target frequency. The characteristics of GAM–PC were evaluated and verified by numerical simulations and practical experiments. The conclusions are summarized as follows:

(1) The proposed GAM–PC device demonstrates superior amplification of acoustic signal amplitude, outperforming the GAM gradient model without an incorporated phonon crystal structure;
(2) Compared with the conventional gradient model, GAM–PC can operate at a lower frequency without any change in volume;
(3) Each slit of the GAM–PC structure has a narrower bandwidth, which makes the structure more frequency selective;
(4) The structure has the ability to separate different frequency components, which can be applied to signal monitoring in noisy and complex environments;
(5) The GAM–PC structure can be designed flexibly for relevant frequency bands, indicating its potential for practical applications in sensing enhancement across various research fields. The study also identifies topics for future research, such as multi-band fusion, integration with electronics, and manufacturing simplification.

Author Contributions: Conceptualization, X.Z. and Y.S.; methodology, G.H.; software, X.Z.; validation, X.Z.; formal analysis, X.Z.; investigation, G.H.; resources, Y.S. and J.H.; data curation, X.Z.; writing—original draft preparation, X.Z.; writing—review and editing, J.H.; visualization, G.H.; supervision, Y.S.; project administration, Y.S. and J.H.; funding acquisition, J.H. All authors have read and agreed to the published version of the manuscript.

Funding: This research was funded by National Key R&D Program of China, grant number 2023YFE0202800, the Natural Science Foundation of Shanxi Province, grant numbers 202103021224201, 202203021211100, and 201901D211232, and The National Natural Science Foundation of China, grant number 61671414.

Data Availability Statement: The data presented in this study are openly available in web of science.

Acknowledgments: The work was supported by National Key R&D Program of China (2023YFE0202800), Natural Science Foundation of Shanxi Province (202103021224201, 202203021211100, and 201901D211232) and The National Natural Science Foundation of China (61671414).

Conflicts of Interest: The authors declare no conflict of interest. The funders had no role in the writing of the manuscript nor in the decision to publish the results.

References

1. Miniaci, M.; Gliozzi, A.S.; Morvan, B.; Krushynska, A.; Bosia, F.; Scalerandi, M. Proof of Concept for an Ultrasensitive Technique to Detect and Localize Sources of Elastic Nonlinearity Using Phononic Crystals. *Phys. Rev. Lett.* **2017**, *118*, 214301. [PubMed]
2. Danawe, H.; Okudan, G.; Ozevin, D.; Tol, S. Conformal gradient-index phononic crystal lens for ultrasonic wave focusing in pipe-like structures. *Appl. Phys. Lett.* **2020**, *117*, 021906.
3. Cabada, E.C.; Leclere, Q.; Antoni, J.; Hamzaoui, N. Fault detection in rotating machines with beamforming: Spatial visualization of diagnosis features. *Mech. Syst. Signal Process.* **2017**, *97*, 33–43.
4. Tian, Y.; Wei, Q.; Cheng, Y.; Liu, X.J. Acoustic holography based on composite metasurface with decoupled modulation of phase and amplitude. *Appl. Phys. Lett.* **2017**, *110*, 191901.
5. Wu, G.; Hu, X.; Liu, X.; Dong, Z.; Yue, Y.; Cai, C. Fabrication of Glass Diaphragm Based Fiber-Optic Microphone for Sensitive Detection of Airborne and Waterborne Sounds. *Sensors* **2022**, *22*, 2218.
6. Cho, K.; Okumura, H.; Nishiura, T.; Yamashita, Y. Multiple Sound Source Localization Based on Inter-Channel Correlation Using a Distributed Microphone System in a Real Environment. *IEICE Trans. Inf. Syst.* **2010**, *E93D*, 2463–2471.
7. Cummer, S.A.; Christensen, J.; Alu, A. Controlling sound with acoustic metamaterials. *Nat. Rev. Mater.* **2016**, *1*, 16001.
8. Zigoneanu, L.; Popa, B.-I.; Cummer, S.A. Three-dimensional broadband omnidirectional acoustic ground cloak. *Nat. Mater.* **2014**, *13*, 352–355.
9. Zhu, J.; Christensen, J.; Jung, J.; Martin-Moreno, L.; Yin, X.; Fok, L. A holey-structured metamaterial for acoustic deep-subwavelength imaging. *Nat. Phys.* **2011**, *7*, 52–55.
10. Hu, C.J.; Xue, S.W.; Yin, Y.H.; Hao, Z.L.; Zhou, Y.Y.; Chen, H.Y. Acoustic super-resolution imaging based on solid immersion 3D Maxwell's fish-eye lens. *Appl. Phys. Lett.* **2022**, *120*, 192202.
11. Ismail, A.Y.; Kim, J.; Chang, S.M.; Koo, B. Sound transmission loss of a Helmholtz Resonator-based acoustic metasurface. *Appl. Acoust.* **2022**, *188*, 108569. [CrossRef]
12. Peng, Y.Y.; Chen, J.H.; Yang, Z.Z.; Zou, X.Y.; Tao, C.; Cheng, J.C. Broadband tunable acoustic metasurface based on piezoelectric composite structure with two resonant modes. *Appl. Phys. Express* **2022**, *15*, 014004.
13. Zou, H.Z.; Li, P.; Peng, P. An ultra-thin acoustic metasurface with multiply resonant units. *Phys. Lett. A* **2020**, *384*, 126151. [CrossRef]
14. Wei, W.; Chronopoulos, D.; Meng, H. Broadband Vibration Attenuation Achieved by 2D Elasto-Acoustic Metamaterial Plates with Rainbow Stepped Resonators. *Materials* **2021**, *14*, 4759. [CrossRef] [PubMed]
15. Rahman, M.N.; Islam, M.T.; Samsuzzaman, S.M. Resonator based metamaterial sensor to detect unknown materials. *Microw. Opt. Techn. Lett.* **2018**, *60*, 1681–1685.
16. Mei, J.; Ma, G.; Yang, M.; Yang, Z.; Wen, W.; Sheng, P. Dark acoustic metamaterials as super absorbers for low-frequency sound. *Nat. Commun.* **2012**, *3*, 756. [PubMed]
17. Cheng, Y.; Zhou, C.; Yuan, B.G.; Wu, D.J.; Wei, Q.; Liu, X.J. Ultra-sparse metasurface for high reflection of low-frequency sound based on artificial Mie resonances. *Nat. Mater.* **2015**, *14*, 1013–1019.
18. Li, Z.; Wang, X. Wave propagation in a dual-periodic elastic metamaterial with multiple resonators. *Appl. Acoust.* **2021**, *172*, 107582.
19. Xing, T.; Gai, X.; Zhao, J.; Li, X.; Cai, Z.; Guan, X. Low frequency sound absorption of adjustable membrane-type acoustic metamaterials. *Appl. Acoust.* **2022**, *188*, 108586.
20. Popa, B.I.; Cummer, S.A. Non-reciprocal and highly nonlinear active acoustic metamaterials. *Nat. Commun.* **2014**, *5*, 3398. [CrossRef]
21. Li, Y.; Peng, Y.G.; Han, L.; Miri, M.A.; Li, W.; Xiao, M. Anti-parity-time symmetry in diffusive systems. *Science* **2019**, *364*, 170–173. [CrossRef] [PubMed]

22. Xue, H.R.; Yang, Y.H.; Gao, F.; Chong, Y.D.; Zhang, B.L. Acoustic higher-order topological insulator on a kagome lattice. *Nat. Mater.* **2019**, *18*, 108–112. [PubMed]
23. He, H.L.; Qiu, C.Y.; Ye, L.P.; Cai, X.X.; Fan, X.Y.; Ke, M.Z. Topological negative refraction of surface acoustic waves in a Weyl phononic crystal. *Nature* **2018**, *560*, 61–64. [CrossRef] [PubMed]
24. Li, J.S.; Fok, L.; Yin, X.B.; Bartal, G.; Zhang, X. Experimental demonstration of an acoustic magnifying hyperlens. *Nat. Mater.* **2009**, *8*, 931–934. [CrossRef] [PubMed]
25. Ma, G.C.; Yang, M.; Xiao, S.W.; Yang, Z.Y.; Sheng, P. Acoustic metasurface with hybrid resonances. *Nat. Mater.* **2014**, *13*, 873–878. [CrossRef]
26. Wang, Y.F.; Wang, T.T.; Liu, J.P.; Wang, Y.S.; Laude, V. Guiding and splitting Lamb waves in coupled-resonator elastic waveguides. *Compos. Struct.* **2018**, *206*, 588–593.
27. Liang, Z.X.; Li, J.S. Extreme Acoustic Metamaterial by Coiling Up Space. *Phys. Rev. Lett.* **2012**, *108*, 114301. [CrossRef]
28. Chen, Y.Y.; Liu, H.J.; Reilly, M.; Bae, H.; Yu, M.A. Enhanced acoustic sensing through wave compression and pressure amplification in anisotropic metamaterials. *Nat. Commun.* **2014**, *5*, 5247.
29. Zhu, J.; Chen, Y.Y.; Zhu, X.F.; Garcia-Vidal, F.J.; Yin, X.B.; Zhang, W.L. Acoustic rainbow trapping. *Sci. Rep.* **2013**, *3*, 1728. [CrossRef]
30. Colombi, A.; Ageeva, V.; Smith, R.J.; Clare, A.; Patel, R.; Clark, M. Enhanced sensing and conversion of ultrasonic Rayleigh waves by elastic metasurfaces. *Sci. Rep.* **2017**, *7*, 6750. [CrossRef]
31. Wang, X.; Li, J.J.; Yang, J.S.; Chen, B.W.; Liu, S.C.; Chen, Y.Y. Compact acoustic amplifiers based on non-adiabatic compression of sound in metamaterial waveguides. *Appl. Acoust.* **2023**, *204*, 109246.
32. Huang, S.; Lin, Y.; Tang, W.; Deng, R.; He, Q.; Gu, F. Sensing with sound enhanced acoustic metamaterials for fault diagnosis. *Front. Phys.* **2022**, *10*, 1027895.
33. Huang, X.; Yan, Y.; Ma, J.; Li, J.; Rui, X. An Acoustic Metamaterial-Based Sensor Capable of Multiband Filtering and Amplification. *IEEE Sens. J.* **2020**, *20*, 4413–4419.
34. Chen, T.; Wang, C.; Yu, D. Pressure amplification and directional acoustic sensing based on a gradient metamaterial coupled with space-coiling structure. *Mech. Syst. Signal Process.* **2022**, *181*, 109499.
35. Zangeneh-Nejad, F.; Fleury, R. Acoustic Analogues of High-Index Optical Waveguide Devices. *Sci. Rep.* **2018**, *8*, 10401.
36. Ruan, Y.D.; Liang, X. 2D phononic-crystal Luneburg lens for all-angle underwater sound localization. *Acta Acust.* **2022**, *6*, 12.
37. Allam, A.; Sabra, K.; Erturk, A. 3D-Printed Gradient-Index Phononic Crystal Lens for Underwater Acoustic Wave Focusing. *Phys. Rev. Appl.* **2020**, *13*, 064064.
38. Kock, W.E.; Harvey, F.K. Refracting Sound Waves. *J. Acoust. Soc. Am.* **1949**, *21*, 471–481.
39. Xia, B.; Wang, G.; Zheng, S. Robust edge states of planar phononic crystals beyond high-symmetry points of Brillouin zones. *J. Mech. Phys. Solids* **2019**, *124*, 471–488.